

Efficient and Stable CsPbI₃ Solar Cells via Regulating Lattice Distortion with Surface Organic Terminal Groups

Tianhao Wu, Yanbo Wang, Zhensheng Dai, Danyu Cui, Tao Wang, Xiangyue Meng, Enbing Bi, Xudong Yang, and Liyuan Han*

All-inorganic cesium lead iodide perovskites (CsPbI₃) are promising wide-bandgap materials for use in the perovskite/silicon tandem solar cells, but they easily undergo a phase transition from a cubic black phase to an orthorhombic yellow phase under ambient conditions. It is shown that this phase transition is triggered by moisture that causes distortion of the corner-sharing octahedral framework ([PbI₆]⁴⁻). Here, a novel strategy to suppress the octahedral tilting of [PbI₆]⁴⁻ units in cubic CsPbI₃ by systematically controlling the steric hindrance of surface organic terminal groups is provided. This steric hindrance effectively prevents the lattice distortion and thus increases the energy barrier for phase transition. This mechanism is verified by X-ray diffraction measurements and density functional theory calculations. Meanwhile, the formation of an organic capping layer can also passivate the surface electronic trap states of perovskite absorber. These modifications contribute to a stable power conversion efficiency (PCE) of 13.2% for the inverted planar perovskite solar cells (PSCs), which is the highest efficiency achieved by the inverted-structure inorganic PSCs. More importantly, the optimized devices retained 85% of their initial PCE after aging under ambient conditions for 30 days.


Organic–inorganic hybrid perovskite solar cells (PSCs) are a promising photovoltaic technology that has made unprecedented progress in recent years.^[1–4] By now, the highest certified power conversion efficiency (PCE) has exceeded 23%, which is comparable to that of state-of-the-art crystalline silicon solar cells.^[5] However, the volatility of the organic components in organic–inorganic hybrid perovskites has become a serious constraint on the long-term stability of PSCs and optoelectronic devices.^[6–8] All-inorganic perovskite materials are among the most promising candidates for overcoming the organic cation–related long-term

stability issue, and much effort has therefore been devoted to development of all-inorganic halide perovskites.^[9,10] All-inorganic cesium lead halide perovskites (CsPbX₃, X = I, Br, Cl) have the advantage over organic–inorganic metal halide perovskites of being more thermally stable because of the replacement of volatile organic cations with cesium ions. Among these lead-halide perovskites, cesium lead iodide (CsPbI₃) perovskite has a bandgap of 1.72 eV, which is ideal for photovoltaic applications, especially for the top cell of perovskite/silicon tandem solar cells.^[11–13] Typically, the inverted structure PSCs were often used in tandem solar cells with high efficiency.^[14] However, the researchers mainly focus on the normal structure in the field of all-inorganic PSCs, the inverted-structure devices were rarely studied and their stabilized efficiency still remains at about 12%.^[15]

Although CsPbI₃ has the most suitable bandgap, the black phase of CsPbI₃ exhibits an undesirable tolerance factor with poor phase stability, which results in automatic transformation to a nonphotoactive yellow phase with a wide bandgap of 2.82 eV after exposure to humid conditions.^[16] Several methods have been exploited to stabilize the black phase of CsPbI₃. Those methods have included doping with Br, exploiting the quantum dots effect, and use of 2D/3D heterojunction structures.^[15,17–20] Nevertheless, these strategies would undesirably broaden the bandgap, hinder carrier transport, and lead to mismatched band alignment with the charge extraction layer. The result would be a decrease of light absorption and unfavorable charge recombination.^[21] Moreover, the solution-processed CsPbI₃ films often present a high content of metallic Pb cluster (Pb⁰) acting as electron-based trap state on the surface,^[17] which may induce serious charge recombination in the perovskite/electron transporting layer interface, and thus limit the performance of PSCs with an inverted configuration. Surface organic capping layer would be an effective way to stabilize the CsPbI₃ black phase and further improve the device performance through efficient passivation of the surface ionic defects.^[22] So far, many organic ligands composed of anchoring functional groups and bulk alkyl chains have been employed to form a surface capping layer for phase stabilization of CsPbI₃ perovskite, including oleylamine, oleic acid, acetic acid, poly(vinylpyrrolidone), sulfobetaine zwitterions, and phenethylammonium iodide.^[23–25]

Dr. T. Wu, Dr. Y. Wang, Dr. Z. Dai, Dr. D. Cui, Dr. T. Wang, Dr. E. Bi, Prof. X. Yang, Prof. L. Han
State Key Laboratory of Metal Matrix Composites
Shanghai Jiao Tong University
800 Dong Chuan Road, Shanghai 200240, China
E-mail: Han.liyuan@sjtu.edu.cn

Dr. X. Meng, Prof. L. Han
Photovoltaic Materials Group
Center for Green Research on Energy and Environmental Materials
National Institute for Materials Science
Tsukuba, Ibaraki 305-0047, Japan

 The ORCID identification number(s) for the author(s) of this article can be found under <https://doi.org/10.1002/adma.201900605>.

DOI: 10.1002/adma.201900605

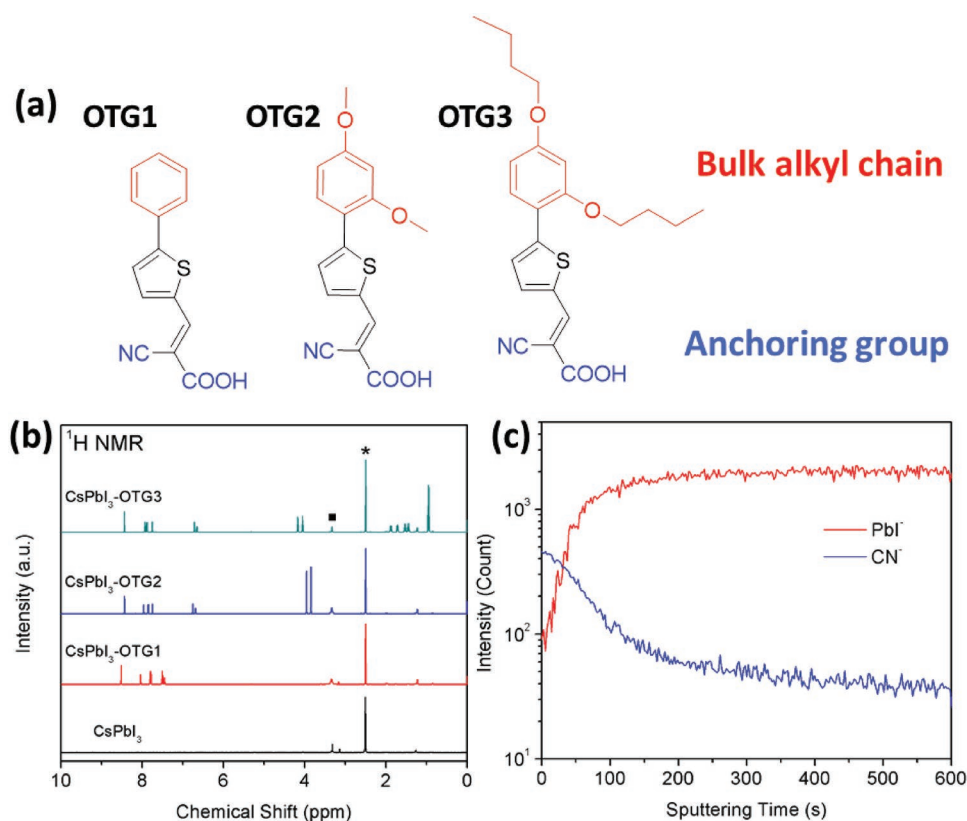


Figure 1. a) Chemical structures of OTG1, OTG2, and OTG3. b) Liquid-state ^1H NMR spectrum of the relative perovskite samples, characteristic peaks of the DMSO solvent and residual water are marked with asterisk and solid square, respectively. c) TOF-SIMS profiles showing Pbi^- and CN^- components from the top to the bottom of the CsPbI_3 -OTG3 film.

However, this ligand-induced phase stabilization usually causes a smaller grain size in the CsPbI_3 perovskite films,^[26,27] which still limits the solar cells performance. Therefore, more efforts are needed to take the phase stability and the photovoltaic performance of CsPbI_3 PSCs into consideration simultaneously, which could be achieved by a rational design of the organic ligand and a comprehensive study on the phase-stabilizing mechanism of CsPbI_3 perovskite.

In this study, we fabricated the inverted planar CsPbI_3 based PSCs and found that increasing the steric hindrance of organic ligand could significantly improve the phase stability of CsPbI_3 perovskite by suppressing the lattice distortion triggered by moisture or polar solvents. The bulky organic ligands serving as organic terminal groups (OTGs) are used in this work. Three OTG molecules (OTG1, OTG2, and OTG3) were designed with different substituted phenyl units (phenyl, 2,4-dimethoxy phenyl, and 2,4-dibutoxy phenyl) as bulk alkyl chains, cyanoacetic acid as an anchor for bonding with the Pb–I framework of perovskite lattice. Besides, thiophene based π -spacer is employed to keep the molecular planarity and enhance intramolecular π – π interaction due to the small resonance energy of thienyl segment, which is considered to suppress the thermal decomposition of OTG molecules under high-temperature annealing process.^[28] **Figure 1a** shows the chemical structures of three such molecules. The X-ray diffraction (XRD) measurements and density functional theory (DFT) calculations

demonstrated that a large 2,4-dibutoxy phenyl unit applied in OTG3 could efficiently hinder the octahedral tilting of the corner-sharing $[\text{PbI}_6]^{4-}$ black phase through a strong steric-hindrance effect. Such effect increases the formation energy of orthorhombic yellow phase with an edge-sharing $[\text{PbI}_6]^{4-}$ structure. Moreover, the fact that the carboxylate group on OTG molecules passivated the surface Pb^0 defects further reduced the nonradiative recombination of charge carriers in perovskite layer.^[29] Consequently, the stable power conversion efficiency of PSCs with a surface organic capping layer reached 13.2% for the inverted planar structure. More importantly, CsPbI_3 PSCs with an OTG3 capping layer showed much higher phase stability against moisture than did the pristine CsPbI_3 devices. The CsPbI_3 -OTG3 device retained 85% of its initial PCE after aging for 30 days in ambient air without encapsulation. These results emphasize the importance of regulating lattice distortion to produce efficient and stable all-inorganic CsPbI_3 PSCs.

OTG1, OTG2, and OTG3 molecules were synthesized by procedures described in our previous reports,^[30] the steps of synthesis are shown in Figure S1a (Supporting Information). Figure S1b (Supporting Information) provides the thermogravimetric analysis (TGA) of OTG1, OTG2, and OTG3. All the samples exhibit negligible weight loss associated with the decomposition or thermal evaporation of OTG molecules from 20 to 200 °C, indicating their good thermal stability for the application of CsPbI_3 based devices. The surface passivation

process of CsPbI₃ perovskite was conducted by adding OTG molecules to a perovskite precursor solution composed of CsI and HPbI₃. The perovskite black phase was formed after a one-step spin-coating procedure and gradient thermal annealing at 90 and 150 °C. The formation of the black phase was attributed to the fact that the HPbI₃ intermediate could facilitate transition to the CsPbI₃ black phase at lower temperature than that of the traditional method used CsI and PbI₂ as precursor.^[31] Details of the process are provided in the experimental section. Figure S2 (Supporting Information), which shows the XRD pattern of pristine HPbI₃ powder used in perovskite precursor, depicts the strong peaks at 11.7°, 25.9°, and 31.3° associated with the (100), (201), and (310) planes, respectively, of the HPbI₃ crystal.^[11]

In order to verify the presence of OTG molecules in the CsPbI₃ film after thermal annealing process, we redissolved the perovskite films in d₆-DMSO solvent for nuclear magnetic resonance (NMR) measurement. ¹H NMR spectrums of the relative samples are plotted in Figure 1b. The corresponding peaks in CsPbI₃-OTG samples are assigned to the H atoms presented on cyanoacetic acid (8.4–8.5 ppm), thiophene π -spacer (7.7–8.0 ppm), phenyl unit (6.7–7.5 ppm), and the bulk alkyl chain (0.9–4.2 ppm), respectively. Besides, some works indicate that HPbI₃ precursor may introduce extra organic cations called dimethylammonium (DMA) into the CsPbI₃ perovskite lattice.^[32] However, the ¹H NMR peaks at 8.2 and 2.7 ppm assigned to the amino (–NH₂⁺) and methyl (–CH₃) groups of DMA cation (¹H NMR of DMAI is shown in Figure S3 in the Supporting Information), respectively, are absent in our perovskite samples. Based on this result, we deduce that the perovskite film fabricated by this work is all-inorganic rather

than the organic–inorganic hybrid one. Additionally, we employ time-of-flight secondary-ion mass spectrometry (TOF-SIMS) analysis (Figure 1c) to investigate the vertical distribution of OTG molecules (indicated by CN[–]) in CsPbI₃ film (indicated by PbI[–]), which indicates that OTG molecules mainly serve as a surface organic capping layer on the CsPbI₃ perovskite.

The coordinated reaction between the carboxylate (O=C–O) of OTG molecules and CsPbI₃ perovskite was demonstrated via Fourier transform infrared (FTIR) spectroscopy. Figure S4a (Supporting Information) shows the FTIR spectra of OTG molecules and the CsPbI₃-OTG mixture. The stretching vibration of the C=O bond in pure OTG3 was observed at 1685 cm^{–1}. The C=O vibration was shifted to a lower wavenumber of 1671 cm^{–1} in the CsPbI₃-OTG3 mixture. The other peaks presented in 1260, 1302, 1425, and 1579 cm^{–1} are relative to the vibration signal of Ar–H, C–O–C, C–H, and C=C bonds in the OTG molecules. In addition, X-ray photoelectron spectroscopy (XPS) analysis further confirms the coordination between carboxylate and Pb²⁺ cations, as shown in Figure S4b (Supporting Information). The XPS O 1s spectrum revealed three clear peaks at 529.4 eV (Pb–O bond), 531.5 eV (C=O bond), and 532.8 eV (C–O bond), in contrast to the single peak at 531.3 eV (absorption of the water molecules) for pristine CsPbI₃ film.^[33,34]

To study the effect of OTG molecules on the crystallization process of CsPbI₃ perovskite, we compared the XRD patterns of pristine CsPbI₃ and the CsPbI₃-OTG films (Figure 2a). The main diffraction peaks of pristine CsPbI₃ appeared at 14.4°, 20.6°, and 28.9°. We attributed them to the preferred orientations of (110), (020), and (220), respectively. The split peaks of the (002), (112), and (004) orientations were related to the

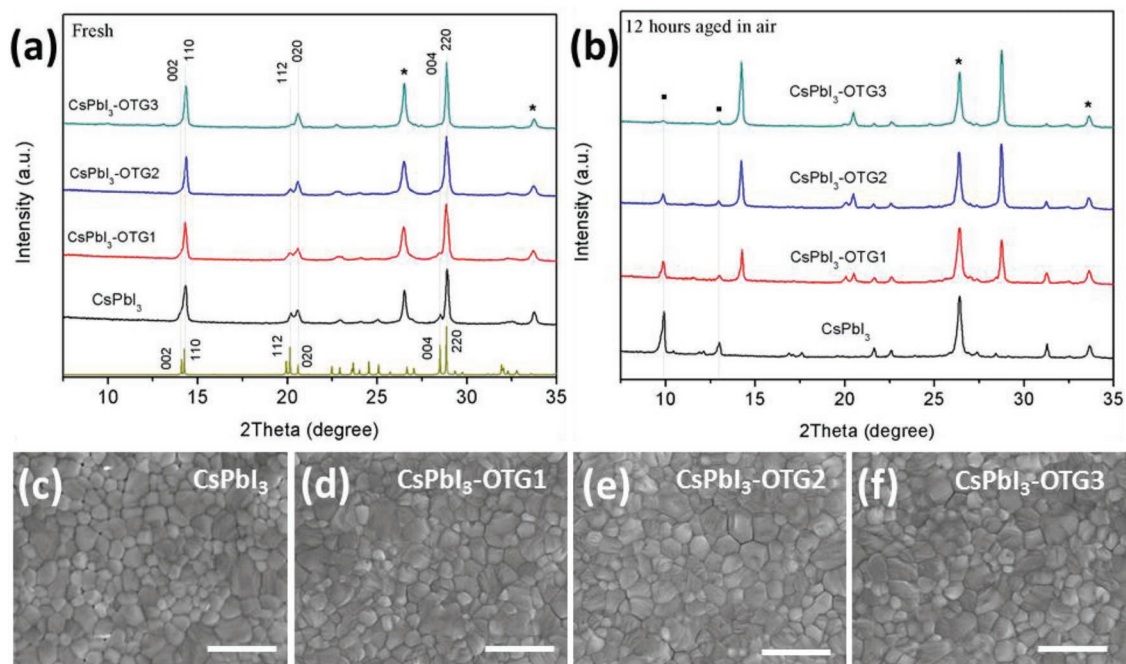


Figure 2. a,b) XRD patterns of the corresponding perovskite films deposited on fluorine-doped tin oxide (FTO)-coated glass before (a) and after (b) being aged in air (50–60% relative humidity) for 12 h. The diffraction peaks of the FTO substrate are marked with an asterisk, and the diffraction peaks of the CsPbI₃ yellow phase are marked with a solid square. c–f) Top-view scanning electron microscopy images of pristine CsPbI₃ (c), CsPbI₃-OTG1 (d), CsPbI₃-OTG2 (e), and CsPbI₃-OTG3 films (f). The scale bar indicates 1 μm.

presence of the distorted corner-sharing $[\text{PbI}_6]^{4-}$ structure (γ - CsPbI_3 , orthorhombic black phase) with a Pb–I–Pb bond angle of 155.6° . This structure is frequently found in the CsPbI_3 perovskite processed with HPbI_3 or HI in the precursor solution.^[35,36] Interestingly, the CsPbI_3 -OTG films exhibited an obvious decrease of peak intensity for the (002), (112), and (004) planes, especially in the case of CsPbI_3 -OTG3. These observations further point to the fact that fabrication of large steric hindrance terminal groups on the CsPbI_3 surface is critical for suppressing the octahedral tilting of $[\text{PbI}_6]^{4-}$ units in the perovskite lattice. In addition, the fact that the XRD pattern of the CsPbI_3 -OTG films did not show any additional peaks associated with the 2D structure is attributable to the fact that large organic molecules could not permeate into the perovskite lattice. Besides, the UV–vis spectrum (Figure S5, Supporting Information) indicated that the presence of OTG molecules did not affect the UV–vis absorption and the bandgap of CsPbI_3 perovskite.

Figure 2b illustrates the XRD patterns of the corresponding perovskite films after they were kept in moist air for 12 h. For the pristine CsPbI_3 films, the diffraction peaks of the black phase almost disappeared along with the strong peaks located at 9.8° and 12.9° attributable to the presence of the orthorhombic yellow phase.^[21] The fact that the XRD pattern of CsPbI_3 -OTG3 film was very similar to that of the fresh sample indicated that suppressing $[\text{PbI}_6]^{4-}$ octahedral tilting played a vital role in hindering the phase transition of the black phase of CsPbI_3 . Figure S6 (Supporting Information) also shows the color change versus the time of aging of the corresponding perovskite films. The phase-stabilizing effect of OTG molecules under treatment with another polar solvent was also investigated by dipping perovskite films in ethanol. Figure S7 (Supporting Information) shows the XRD patterns of those films. We found that the CsPbI_3 black phase treated with OTG3 also exhibited much higher resistance to phase transition than the black phase of the pristine sample.

We used scanning electron microscopy (SEM) to characterize the impact of OTG molecules on the surface morphology of CsPbI_3 perovskite films. Top-view SEM images of the corresponding perovskite films (Figure 2c–f) revealed little difference in grain size before and after treatment with OTG molecules, as is apparent in the distributions of grain sizes (Figure S8, Supporting Information). Previous reports have demonstrated that minimizing the grain sizes (increasing the surface/volume ratios) is an efficient way to stabilize the CsPbI_3 black phase. The fact that the highly symmetrical cubic structure usually has a surface energy smaller than that of the orthorhombic structure leads to a reduction of the total Gibbs free energy of the material surface.^[37] This observation confirms that the mechanism of phase stabilization of OTG molecules is not associated with reduction of the grain size of CsPbI_3 perovskite. In addition, we used energy dispersive spectrometry (EDS) to determine the distribution of elements in the modified perovskite films. Figure S9 (Supporting Information) shows the element mapping profiles of CsPbI_3 -OTG3 films.

Figure 3a illustrates the phase stabilizing mechanism of CsPbI_3 perovskite with OTG molecules as the surface capping layer. First, OTG molecules in the precursor solution are thought to act as nucleation sites for the growth of the cubic

CsPbI_3 black phase. This step is followed by formation of a perovskite film with a surface OTG capping layer. After exposure to moisture or another polar solvent, the bulk alkyl chains of the OTG molecules provide steric hindrance that suppresses the tilting of the $[\text{PbI}_6]^{4-}$ octahedron frameworks, resulting in hindrance of the phase transition to the orthorhombic phase. We also performed DFT calculations to better understand the moisture-induced lattice distortion of cubic CsPbI_3 . We simulated the interaction between H_2O molecules and cubic CsPbI_3 containing three-layer $[\text{PbI}_6]^{4-}$ octahedral units without and with OTG1, OTG2, and OTG3 at the lattice surface. The generalized gradient approximation in the form of Perdew–Burke–Ernzerhof was used for the exchange–correlation function.^[38] Figure 3b–e shows the geometry-optimized structures. It is apparent that the surface Cs^+ ions moved from their original positions and approached H_2O molecules in pristine CsPbI_3 . This change in position induced a shift of the electron cloud associated with the Cs^+ ions and thus caused a tilting of the adjacent corner-sharing $[\text{PbI}_6]^{4-}$ frameworks. This result is similar to the prediction of a previous theoretical calculation based on the ethanol molecule.^[39] In contrast, the theoretical model of CsPbI_3 -OTG, which contains large bulk alkyl groups, showed much less lattice distortion, especially in the case of CsPbI_3 -OTG3. The Pb–I–Pb bond angle indicated in Figure S10 (Supporting Information) is 134.5° in pristine CsPbI_3 . This angle is much smaller than the angle of the corner-sharing $[\text{PbI}_6]^{4-}$ frameworks in the cubic phase (180°) and approaches the angles of the edge-sharing $[\text{PbI}_6]^{4-}$ frameworks in the orthorhombic phase (91.4° and 95.1°). Interestingly, this bond angle increases to 157.8° , 170.2° , and 179.4° in the CsPbI_3 -OTG1, CsPbI_3 -OTG2, and CsPbI_3 -OTG3 models, respectively. Other calculations illustrate that the decrease of the Pb–I–Pb bond angle gives rise to a weaker antibonding state with the overlapping Pb–I orbitals. This characteristic has been shown to cause a reduction of the defect tolerance of CsPbI_3 perovskite, which is undesirable for high-performance PSCs.^[40] This calculated result is consistent with our experimental results and highlights the importance of regulating CsPbI_3 lattice distortion to achieve stable and efficient all-inorganic PSCs.

To investigate the impact of the organic capping layer on the surface defect states, we used XPS to examine the Pb 4f core levels of CsPbI_3 and CsPbI_3 -OTG3 (Figure 4a). The dominant peaks (138.0 eV for $4f_{7/2}$ and 143.1 eV for $4f_{5/2}$) were associated with Pb^{2+} atoms with a saturated coordination, and we attributed the small peaks (asterisks in Figure 4a) at lower binding energy (136.9 eV for $4f_{7/2}$ and 142.0 eV for $4f_{5/2}$) to the defects of undercoordinated Pb^{2+} ions that were associated with the metallic Pb cluster (Pb^0).^[41] Theoretical computations and experimental studies have indicated that the Pb^0 defects are the main source of electronic trap states and serves as a nonradiative recombination center for charge carriers.^[42] By calculating the peak area ratio of Pb^0 to Pb 4f, we could estimate the content of Pb^0 to be 4.13 at% and 0.65 at% for CsPbI_3 and CsPbI_3 -OTG3, respectively. This result implies that the organic capping layer could significantly reduce the density of defects on the CsPbI_3 surface. Furthermore, we calculated the electronic trap density of perovskite film by measuring dark current–voltage (I – V) curves of the electron-only devices with a structure of FTO/ TiO_2 /perovskite/PCBM/Ag electrode. Figure 4b depicts

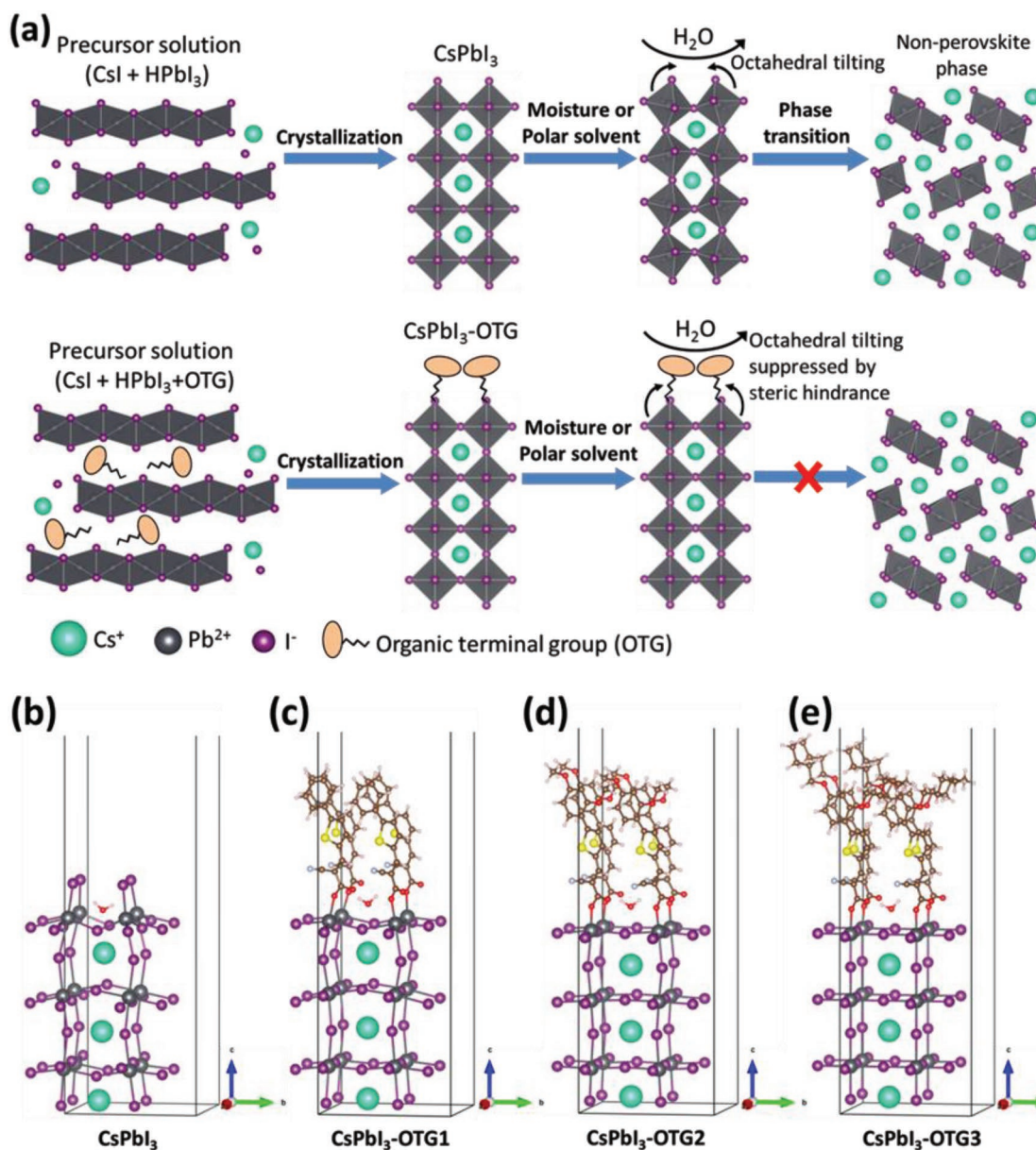


Figure 3. a) Mechanism of the OTG-induced phase stabilization of CsPbI₃ perovskite. b–e) The geometry-optimized structure of water molecules adsorbed onto CsPbI₃ (b), CsPbI₃-OTG1 (c), CsPbI₃-OTG2 (d), and CsPbI₃-OTG3 (e) with three layers of [PbI₆]⁴⁻ units. The light green, gray, and purple spheres represent Cs, Pb, and I atoms, respectively.

the dark *I*-*V* curves of CsPbI₃ and CsPbI₃-OTG3-based devices, which include an Ohmic regime, a trap-filled limited regime and a trap-free space charge limited current (SCLC) regime. The trap density can be deduced from the onset voltage of the trap-filled limit region (V_{TFL}), as depicted in Equation (1):

$$N_{\text{trap}} = \frac{2\epsilon_0\epsilon_r V_{\text{TFL}}}{ql^2} \quad (1)$$

where ϵ_0 is the vacuum permittivity, ϵ_r is the relative dielectric constant, q is the charge constant, and l is the thickness of the perovskite film. It is found that the trap density significantly decreases from 2.02×10^{16} to $8.75 \times 10^{15} \text{ cm}^{-3}$ for the control

and passivated devices, which is consistent with the XPS analysis.

Figure 4c displays the steady-state photoluminescence (PL) spectrum of CsPbI₃ and CsPbI₃-OTG3 perovskite films coated on bare glass. The fact that the PL intensity of CsPbI₃-OTG3 was much higher and that the PL peaks were slightly blue shifted (from 722 to 719 nm) indicated that passivation of surface electronic trap states had occurred.^[43] Furthermore, the fact that PL quenching of the PCBM-coated CsPbI₃ film changed very little after the passivation process (Figure S11, Supporting Information) implied that the surface-capping OTG3 molecules did not affect the interface charge extraction efficiency of the charge-transporting layer. Figure 4d shows the time-resolved

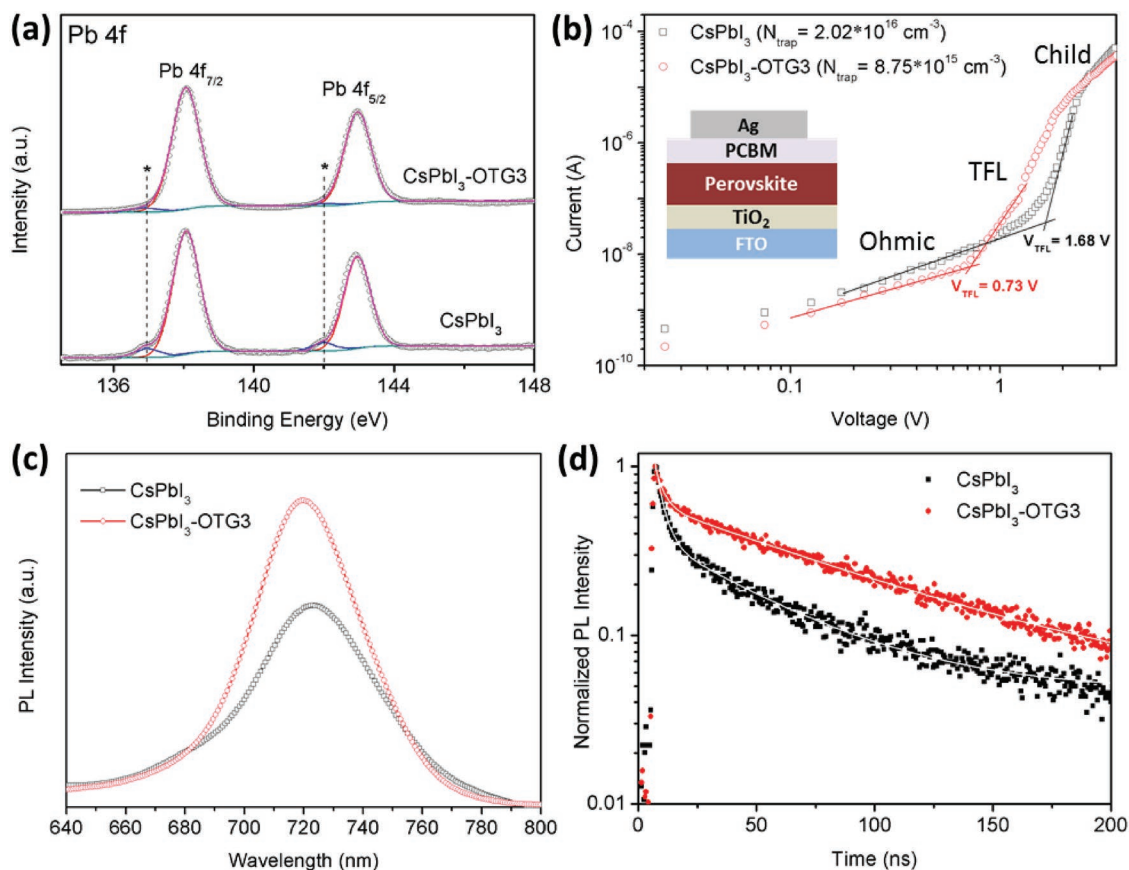


Figure 4. a) X-ray photoelectron spectroscopy analysis of Pb 4f core levels. b) Dark I - V plot of the electron-only perovskite device, the device configuration is depicted in the inset. Three regions can be identified based on the slope (n) of the curve: $n = 1$ is the Ohmic region, $n = 2$ is the SCLC region (child), and $n > 3$ is the trap-filled limited region (TFL). c) Steady-state photoluminescence spectra and d) time-resolved PL decays for the CsPbI₃ and CsPbI₃-OTG3 films. The asterisks indicate the presence of Pb⁰ components. The samples for PL measurement were deposited on bare glass substrates.

PL plot of the corresponding perovskite samples. The PL decay curves were fitted with a double exponential equation, and the parameters derived from the curves are summarized in Table S1 (Supporting Information). The results showed that the fast decay lifetime (τ_1) that accounts for bimolecular recombination of photogenerated free carriers was not obviously changed, but the slow decay lifetime (τ_2) relative to the trap-assisted recombination exhibited a much higher value (81.7 ns) for the CsPbI₃-OTG3 perovskite than for pristine CsPbI₃ (47.4 ns). This enhanced PL lifetime suggests that there was less nonradiative recombination and a lower trap density in the CsPbI₃-OTG3 perovskite films.^[44]

To further study the effect of surface organic terminal groups on the photovoltaic performance of the device, we fabricated perovskite solar cells with an inverted planar structure of fluorine-doped tin oxide (FTO)-coated glass/PTAA/CsPbI₃ perovskite (without or with OTG molecules)/PCBM/BCP/Ag (Figure 5a). Table S2 and Figure S12 (Supporting Information) list the statistic distribution of corresponding photovoltaic parameters (J_{sc} , V_{oc} , FF, and PCE) of the devices with different molar ratios of OTG3 to HPbI₃ in the precursor solution (12 devices in a batch), and the characteristic J - V curves are plotted in Figure S13 (Supporting Information). As the OTG3 molar ratio was increased from 0.1% to 1%, the PCE first increased and

then decreased. The best cell efficiency occurred at a molar ratio of 0.2%. Figure 5b shows the J - V curves of the best devices based on CsPbI₃ and CsPbI₃-OTG3 perovskite. The control devices gave a V_{oc} of 1.07 V, a J_{sc} of 15.85 mA cm⁻², a fill factor (FF) of 68.52%, and a PCE of 11.62%. The performance of the PSCs based on CsPbI₃-OTG3 was an enormous improvement over the performance of the control device; the V_{oc} was 1.12 V, the J_{sc} was 15.81 mA cm⁻², the FF was 75.19%, and the PCE was 13.32%. To increase the accuracy of photovoltaic measurement, we perform the hysteresis analysis of PSCs based on different scan directions (Figure S14, Supporting Information), both the CsPbI₃ and CsPbI₃-OTG3 devices show a negligible hysteresis between forward and reverse scan. The cross-section SEM image of the optimized CsPbI₃-OTG3 device is shown in Figure S15 (Supporting Information). We attributed the enhancements of the V_{oc} and FF of the CsPbI₃-OTG3 PSCs to the efficient passivation of surface electronic trap states caused by the undercoordinated Pb²⁺ defects, which effectively reduced the energy loss due to nonradiative recombination of the charge carrier.

To ensure the reliability of the performance of the device, we measured the steady-state PCE for about 600 s under a constant bias of 0.88 V derived from the maximum power point (P_{max}) (Figure 5c). The stable efficiency of 13.2% that could be

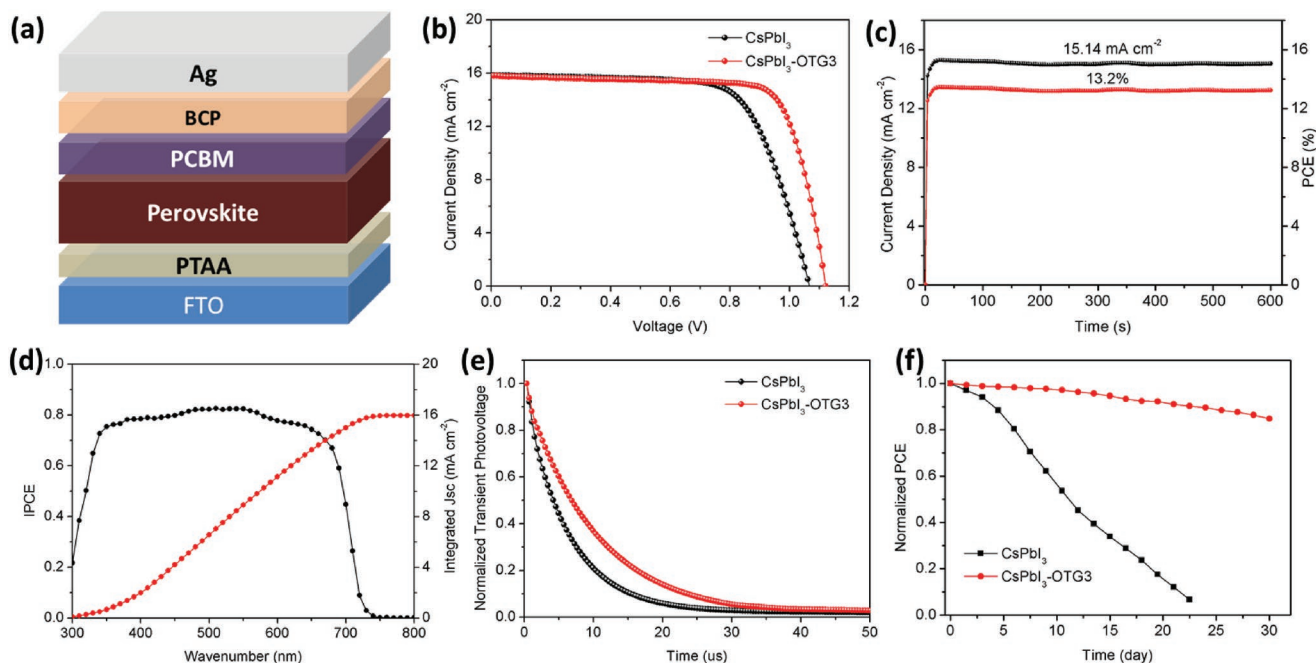


Figure 5. a) Configuration of the perovskite solar cells. b) J - V plots of the best devices based on CsPbI_3 and CsPbI_3 -OTG3 perovskite measured under simulated AM 1.5G solar illumination of 100 mW cm^{-2} in reverse scan. The active area was 0.09 cm^2 for the testing device. c) Stable output curves of the best CsPbI_3 -OTG3 device. d) Internal photon-to-current efficiency (IPCE) of the best CsPbI_3 -OTG3 PSCs. e) Normalized transient photovoltage for CsPbI_3 and CsPbI_3 -OTG3 devices. f) Power conversion efficiency decays of the best CsPbI_3 and CsPbI_3 -OTG3 devices as a function of storage time in dark cabinet with a relative humidity less than 10% at room temperature.

achieved with the best CsPbI_3 -OTG3 PSCs was very consistent with the PCE obtained from the J - V measurements. In contrast, the internal photon-to-current efficiency spectrums for the best CsPbI_3 -OTG3 device (Figure 5d) suggested that the incorporation of OTG3 had little influence on the charge extraction efficiency of the PSCs. The integrated current density was calculated to be 15.87 mA cm^{-2} , in good agreement with the J_{sc} obtained from the J - V characterization. To investigate the charge carrier dynamics in perovskite solar cells, we carried out a transient photovoltage (TPV) analysis to characterize the charge recombination lifetime in the PSCs (Figure 5e). The fact that the rate of decay of the TPV was substantially slower in the CsPbI_3 -OTG3 device ($\tau = 9.64 \mu\text{s}$) than in the CsPbI_3 ($\tau = 5.93 \mu\text{s}$) further explains the reduced charge recombination and improvement of V_{oc} in the CsPbI_3 -OTG3 PSCs.

In addition to its higher photovoltaic performance, the PSCs based on CsPbI_3 -OTG3 also exhibited better stability than those based on CsPbI_3 when kept in a dark cabinet with the relative humidity (RH) less than 10% at room temperature (Figure 5f). The device based on CsPbI_3 -OTG3 without any encapsulation still retained about 85% of its initial PCE after being aged for 30 days. Nevertheless, the PCE of the CsPbI_3 -based device dropped rapidly, the device degraded completely after 3 weeks of storage with the perovskite layer slowly changed to light yellow. Besides, further experiment is conducted to reveal the device stability in a high-humidity condition. As illustrated in Figure S16 (Supporting Information), the CsPbI_3 -OTG3 device also exhibits a small PCE loss of 16% after aging for 7 days in 35–40% RH, but the control one degraded in just 1 day. In addition, the device based on CsPbI_3 -OTG3 maintained 88% of its initial PCE after

200 h of exposure to light in dry air and was therefore much more stable than the device based on CsPbI_3 without an OTG capping layer (Figure S17, Supporting Information).

In summary, we first proposed a strategy to stabilize the black phase of all-inorganic CsPbI_3 perovskite that involved systematically controlling the distortion of the corner-sharing $[\text{PbI}_6]^{4-}$ framework via a large steric effect associated with organic terminal groups. Theoretical calculations and experimental studies demonstrated that the steric hindrance due to the organic terminal groups could maintain the linearity of the Pb–I–Pb bonds and thus suppress the octahedral tilting of adjacent $[\text{PbI}_6]^{4-}$ units in CsPbI_3 . The phase transition resistance against moisture or polar solvents was thereby significantly increased. Moreover, organic terminal groups could also passivate the surface electronic trap states via efficient coordination between carboxylate moieties and undercoordinated Pb^{2+} defects. The result was an extension of the carrier recombination lifetime of the perovskite absorber. By the modification of CsPbI_3 perovskite layer with OTG molecules, we achieved a stabilized PCE of 13.2% for the inverted planar PSCs, which is the highest efficiency obtained by the all-inorganic PSCs with an inverted structure. In addition, the stability of the optimized device in an ambient environment was excellent and superior to that of the pristine device. We believe that this work also provides new insight into the phase-stabilizing mechanism of CsPbI_3 perovskite that will lead toward highly efficient and stable perovskite solar cells. Further study should be done to investigate the impact of organic terminal groups on the stability and photovoltaic performance of all-inorganic perovskite solar cells based on other types of absorbers such as CsPbI_2Br and CsPbIBr_2 .

Experimental Section

Device Fabrication: The FTO-coated glasses were etched with zinc powder and 1 M HCl to obtain patterned substrates. The patterned substrates were then washed with detergent, deionized water, ethanol, and acetone for 20 min each. After being dried with a stream of N₂, the substrates were treated with an ultraviolet plasma for 30 min to remove organic residues. Then, poly(bis(4-phenyl)(2,4,6-trimethylphenyl)amine) (PTAA) dissolved in toluene at a concentration of 5 mg mL⁻¹ was spin-coated onto the FTO substrate at a speed of 6000 rpm for 30 s, and the substrate was then annealed at 120 °C for 20 min. The perovskite precursor solution composed of 0.8 M HPbI₃ and 0.8 M CsI in *N,N*-dimethylformamide without or with the addition of OTG molecules (0.1–1% in molar ratio) was then stirred at 60 °C overnight, and the resulting solution was spin-coated on the PTAA layer (preheated at 60 °C) at 2000 rpm for 35 s. The substrate was then annealed at 90 °C for 5 min and 150 °C for 20 min. A layer of [6,6]phenyl C61 butyric acid methyl ester (PCBM) was then deposited by spin-coating 25 mg mL⁻¹ of PCBM chlorobenzene solution onto the perovskite film at 800 rpm for 30 s and heating at 70 °C for 10 min. Bathocuproine (BCP) was then coated onto the PCBM layer by depositing 140 μL of methanol-saturated solution drop by drop at 6000 rpm for 30 s followed by annealing at 70 °C for 5 min. All of these steps were conducted in a N₂-protected glove box in which the partial pressures of O₂ and H₂O were less than 0.01 ppm. Finally, a 100 nm layer of silver was thermally evaporated onto the as-prepared films to serve as an electrode under high vacuum (lower than 2 × 10⁻⁴ Pa).

Film Characterization: A field-emission scanning electron microscope (JSM-7800F Prime, JEOL) was used to observe the morphology of the as-obtained perovskite films. The steady-state photoluminescence spectrum was measured with a Horiba Fluoromax-4 fluorescence spectrometer using a 500 nm excitation light source. The time-resolved photoluminescence decay was recorded with a Horiba Fluorolog-3 Time Correlated Single Photon Counting system with the excitation wavelength fixed at 440 nm. The XPS analysis was carried out on a Kratos AXIS Ultra DLD spectrometer with an Al Kα X-ray source. The XRD patterns were measured on a Rigaku Ultima IV powder X-ray diffractometer using Cu Kα radiation source with a scan rate of 5° min⁻¹. The UV–vis absorption spectra of the perovskite samples were recorded with a Shimadzu UV 2450 spectrometer. TGA measurements were conducted on a thermo gravimetric analyzer (Pyris 1 TGA) in the nitrogen atmosphere with a heating rate of 10 °C min⁻¹. Liquid-state ¹H NMR analysis was performed on the 600 MHz nuclear magnetic resonance spectrometer (Avance III600 MHz) using d₆-DMSO as deuterated solvent. ToF-SIMS measurements were performed using the focused ion beam ToF-SIMS spectrometer (GAIA3 GMU Model 2016, Czech). A 30 keV Bi⁺ ion beam was used as the primary ion beam to peel the samples with an analysis area of 5 × 5 μm². The linear voltage sweep analysis used to investigate the space charge limited current curves was performed on a multifunctional electrochemical workstation (Zahner, Germany), with a constant step voltage of 20 mV and a scan window from 0 V to 4 V.

Device Characterization: *J*–*V* curves of the PSCs were measured with a digital source meter (Keithley 2400) under simulated solar illumination of 100 mW cm⁻² (AM 1.5G). The intensity of the light source was determined with a standard silicon reference cell (Wacom Denso Co., Japan). The measurements were conducted by a reverse (from 1.2 to –0.2 V) or forward (from –0.2 to 1.2 V) scan. The step voltage and delay time were fixed at 10 mV and 30 ms, respectively. Monochromatic internal photon-to-current efficiency spectral measurements were characterized by using a monochromatic incident light with an irradiance of 1 × 10¹⁶ photons cm⁻² s⁻¹ in direct-current mode. The TPV measurement was recorded on a multifunctional electrochemical analysis instrument (Zahner, Germany). The emission light was generated by a pulse of white light incident on solar cells under open-circuit conditions. No background light was applied. The photostability of the PSCs was tested with continuous illumination from a white LED lamp (100 mW cm⁻²). The devices were put in a glass dry box with a relative humidity of less than 10%. Ultraviolet light (<420 nm) was cut off with an optical filter.

First-Principles Calculation: Geometry optimizations of the OTG1, OTG2, and OTG3 molecules were conducted on the Gaussian 09 program by using B3LYP and the all-electron double-ξ valence basis sets of 6–31G* with default spin mode at the gas phase.^[45,46] Vibrational frequency calculations were also used to ensure that the optimized structure of the dye molecule had no imaginary frequency. First-principles calculations based on the CsPbI₃–OTG models with water molecule absorption were carried out in the framework of density functional theory as implemented in the Vienna Ab Initio Simulation Package (VASP) program.^[47] The generalized gradient approximation in the form of Perdew–Burke–Ernzerhof was used for the exchange–correlation function.^[38] The plane-wave kinetic energy cutoff was fixed at 380 eV, and the interactions of van der Waals forces were simulated by employing the DFT-D model.^[48] Surface slabs were simulated as PbI₂-terminated (001) slabs in the cubic structure, which has three layers of [PbI₆]⁴⁻ units in total. About 20 Å vacuum space was introduced on the top of each slab surface to reduce the interaction between adjacent slabs.

Supporting Information

Supporting Information is available from the Wiley Online Library or from the author.

Acknowledgements

This work was partially supported by the National Natural Science Foundation of China (Grant Nos. 11574199 and 11674219), the New Energy and Industrial Technology Development Organization (NEDO, Japan), the KAKEHI Grant of Japan (Grant No. 18H02078), the Program for Professor of Special Appointment (Eastern Scholar) at Shanghai Institutions of Higher Learning, and the Natural Science Foundation of Shanghai (17ZR1414800).

Conflict of Interest

The authors declare no conflict of interest.

Keywords

cesium lead iodide, lattice distortion, perovskite solar cells, surface passivation

Received: January 24, 2019

Revised: March 13, 2019

Published online:

- [1] H. S. Kim, C. R. Lee, J. H. Im, K. B. Lee, T. Moehl, A. Marchioro, S. J. Moon, R. H. Baker, J. H. Yum, J. E. Moser, M. Grätzel, N. G. Park, *Sci. Rep.* **2012**, 2, 591.
- [2] H. Chen, F. Ye, W. Tang, J. He, M. Yin, Y. Wang, F. Xie, E. Bi, X. Yang, M. Grätzel, L. Han, *Nature* **2017**, 550, 92.
- [3] Y. Wu, X. Yang, W. Chen, Y. Yue, M. Cai, F. Xie, E. Bi, A. Islam, L. Han, *Nat. Energy* **2016**, 1, 16148.
- [4] F. Ye, H. Chen, F. Xie, W. Tang, M. Yin, J. He, E. Bi, Y. Wang, X. Yang, L. Han, *Energy Environ. Sci.* **2016**, 9, 2295.
- [5] N. J. Jeon, H. Na, E. H. Jung, T. Y. Yang, Y. G. Lee, G. Kim, H. W. Shin, S. Il Seok, J. Lee, J. Seo, *Nat. Energy* **2018**, 3, 682.

- [6] E. Bi, H. Chen, F. Xie, Y. Wu, W. Chen, Y. Su, A. Islam, M. Gratzel, X. Yang, L. Han, *Nat. Commun.* **2017**, *8*, 15330.
- [7] P. Delugas, C. Caddeo, A. Filippetti, A. Mattoni, *J. Phys. Chem. Lett.* **2016**, *7*, 2356.
- [8] H. Back, G. Kim, J. Kim, J. Kong, T. K. Kim, H. Kang, H. Kim, J. Lee, S. Lee, K. Lee, *Energy Environ. Sci.* **2016**, *9*, 1258.
- [9] L. Protesescu, S. Yakunin, M. I. Bodnarchuk, F. Krieg, R. Caputo, C. H. Hendon, R. X. Yang, A. Walsh, M. V. Kovalenko, *Nano Lett.* **2015**, *15*, 3692.
- [10] Z. Li, M. Yang, J. S. Park, S. H. Wei, J. J. Berry, K. Zhu, *Chem. Mater.* **2016**, *28*, 284.
- [11] S. Xiang, Z. Fu, W. Li, Y. Wei, J. Liu, H. Liu, L. Zhu, R. Zhang, H. Chen, *ACS Energy Lett.* **2018**, *3*, 1824.
- [12] R. E. Beal, D. J. Slotcavage, T. Leijtens, A. R. Bowring, R. A. Belisle, W. H. Nguyen, G. F. Burkhard, E. T. Hoke, M. D. McGehee, *J. Phys. Chem. Lett.* **2016**, *7*, 746.
- [13] W. Ahmad, J. Khan, G. Niu, J. Tang, *Sol. RRL* **2017**, *1*, 1700048.
- [14] K. A. Bush, A. F. Palmstrom, Z. J. Yu, M. Boccard, R. Cheacharoen, J. P. Mailoa, D. P. McMeekin, R. L. Z. Hoyer, C. D. Bailie, T. Leijtens, I. M. Peters, M. C. Minichetti, N. Rolston, R. Prasanna, S. Sofia, D. Harwood, W. Ma, F. Moghadam, H. J. Snaith, T. Buonassisi, Z. C. Holman, S. F. Bent, M. D. McGehee, *Nat. Energy* **2017**, *2*, 17009.
- [15] C. Liu, W. Li, C. Zhang, Y. Ma, J. Fan, Y. Mai, *J. Am. Chem. Soc.* **2018**, *140*, 3825.
- [16] S. Dastidar, D. A. Egger, L. Z. Tan, S. B. Cromer, A. D. Dillon, S. Liu, L. Kronik, A. M. Rappe, A. T. Fafarman, *Nano Lett.* **2016**, *16*, 3563.
- [17] Q. Zeng, X. Zhang, X. Feng, S. Lu, Z. Chen, X. Yong, S. A. T. Redfern, H. Wei, H. Wang, H. Shen, W. Zhang, W. Zheng, H. Zhang, J. S. Tse, B. Yang, *Adv. Mater.* **2018**, *30*, 1705393.
- [18] A. Swarnkar, A. R. Marshall, E. M. Sanehira, B. D. Chernomordik, D. T. Moore, J. A. Christians, T. Chakrabarti, J. M. Luther, *Science* **2016**, *354*, 92.
- [19] J. Zhang, D. Bai, Z. Jin, H. Bian, K. Wang, J. Sun, Q. Wang, S. Liu, *Adv. Energy Mater.* **2018**, *8*, 1703246.
- [20] E. M. Sanehira, A. R. Marshall, J. A. Christians, S. P. Harvey, P. N. Ciesielski, L. M. Wheeler, P. Schulz, L. Y. Lin, M. C. Beard, J. M. Luther, *Sci. Adv.* **2017**, *3*, eaao4204.
- [21] Y. Wang, T. Zhang, M. Kan, Y. Li, T. Wang, Y. Zhao, *Joule* **2018**, *2*, 2065.
- [22] X. Zheng, B. Chen, J. Dai, Y. Fang, Y. Bai, Y. Lin, H. Wei, X. C. Zeng, J. Huang, *Nat. Energy* **2017**, *2*, 17102.
- [23] A. Pan, B. He, X. Fan, Z. Liu, J. J. Urban, A. P. Alivisatos, L. He, Y. Liu, *ACS Nano* **2016**, *10*, 7943.
- [24] Y. Wang, T. Zhang, M. Kan, Y. Zhao, *J. Am. Chem. Soc.* **2018**, *140*, 12345.
- [25] Q. Wang, X. Zheng, Y. Deng, J. Zhao, Z. Chen, J. Huang, *Joule* **2017**, *1*, 371.
- [26] Z. Zeng, J. Zhang, X. Gan, H. Sun, M. Shang, D. Hou, C. Lu, R. Chen, Y. Zhu, L. Han, *Adv. Energy Mater.* **2018**, *8*, 1801050.
- [27] B. Li, Y. Zhang, L. Fu, T. Yu, S. Zhou, L. Zhang, L. Yin, *Nat. Commun.* **2018**, *9*, 1076.
- [28] Y. Wu, W. Zhu, *Chem. Soc. Rev.* **2013**, *42*, 2039.
- [29] Y. Lin, L. Shen, J. Dai, Y. Deng, Y. Wu, Y. Bai, X. Zheng, J. Wang, Y. Fang, H. Wei, W. Ma, X. C. Zeng, X. Zhan, J. Huang, *Adv. Mater.* **2017**, *29*, 1604545.
- [30] L. Han, A. Islam, H. Chen, C. Malapaka, B. Chiranjeevi, S. Zhang, X. Yang, M. Yanagida, *Energy Environ. Sci.* **2012**, *5*, 6057.
- [31] K. Wang, Z. Jin, L. Liang, H. Bian, D. Bai, H. Wang, J. Zhang, Q. Wang, L. Shengzhong, *Nat. Commun.* **2018**, *9*, 4544.
- [32] W. Ke, I. Spanopoulos, C. C. Stoumpos, M. G. Kanatzidis, *Nat. Commun.* **2018**, *9*, 4785.
- [33] W. Huang, S. Sadhu, S. Ptasinska, *Chem. Mater.* **2017**, *29*, 8478.
- [34] N. Balis, A. A. Zaky, D. Perganti, A. Kaltzoglou, L. Sygellou, F. Katsaros, T. Stergiopoulos, A. G. Kontos, P. Falaras, *ACS Appl. Energy Mater.* **2018**, *1*, 6161.
- [35] B. Zhao, S. F. Jin, S. Huang, N. Liu, J. Y. Ma, D. J. Xue, Q. Han, J. Ding, Q. Q. Ge, Y. Feng, J. S. Hu, *J. Am. Chem. Soc.* **2018**, *140*, 11716.
- [36] R. J. Sutton, M. R. Filip, A. A. Haghighirad, N. Sakai, B. Wenger, F. Giustino, H. J. Snaith, *ACS Energy Lett.* **2018**, *3*, 1787.
- [37] J. M. McHale, A. Auroux, A. J. Perrotta, A. Navrotsky, *Science* **1997**, *277*, 788.
- [38] G. Kresse, J. Furthmüller, *Comput. Mater. Sci.* **1996**, *6*, 15.
- [39] J. K. Sun, S. Huang, X. Z. Liu, Q. Xu, Q. H. Zhang, W. J. Jiang, D. J. Xue, J. C. Xu, J. Y. Ma, J. Ding, Q. Q. Ge, L. Gu, X. H. Fang, H. Z. Zhong, J. S. Hu, L. J. Wan, *J. Am. Chem. Soc.* **2018**, *140*, 11705.
- [40] Y. Huang, W. J. Yin, Y. He, *J. Phys. Chem. C* **2018**, *122*, 1345.
- [41] W. Zhang, S. Pathak, N. Sakai, T. Stergiopoulos, P. K. Nayak, N. K. Noel, A. A. Haghighirad, V. M. Burlakov, D. W. deQuilettes, A. Sadhanala, W. Li, L. Wang, D. S. Ginger, R. H. Friend, H. J. Snaith, *Nat. Commun.* **2015**, *6*, 10030.
- [42] D. Wei, F. Ma, R. Wang, S. Dou, P. Cui, H. Huang, J. Ji, E. Jia, X. Jia, S. Sajid, A. M. Elseman, L. Chu, Y. Li, B. Jiang, J. Qiao, Y. Yuan, M. Li, *Adv. Mater.* **2018**, *30*, 1707583.
- [43] X. Li, C. C. Chen, M. Cai, X. Hua, F. Xie, X. Liu, J. Hua, Y. T. Long, H. Tian, L. Han, *Adv. Energy Mater.* **2018**, *8*, 1800715.
- [44] Q. Chen, H. Zhou, T. B. Song, S. Luo, Z. Hong, H. S. Duan, L. Dou, Y. Liu, Y. Yang, *Nano Lett.* **2014**, *14*, 4158.
- [45] C. Lee, W. Yang, R. G. Parr, *Phys. Rev. B* **1988**, *37*, 785.
- [46] R. Krishnan, J. S. Binkley, R. Seeger, J. A. Pople, *J. Chem. Phys.* **1980**, *72*, 650.
- [47] G. Kresse, J. Furthmüller, *Phys. Rev. B* **1996**, *54*, 11169.
- [48] P. E. Blöchl, *Phys. Rev. B* **1994**, *50*, 17953.